Research Article | Vol. 9, No. 8 / 1 August 2019 / Optical Materials Express 3342

Optical Materials EXPRESS

Standard red green blue (sRGB) color representation with a tailored dual-resonance mode in metal/dielectric stacks

DO HYEON KIM,[1,2] YOUNG JIN YOO,[1,2] JOO HWAN KO,[1,2] YEONG JAE KIM,[1] AND YOUNG MIN SONG[1,*]

[1] School of Electrical Engineering and Computer Science (EECS), Gwangju Institute of Science and Technology (GIST), 123, Cheomdangwagi-ro, Buk-gu, Gwangju 61005, South Korea
[2] These authors contributed equally to this work and should be considered as co-first authors
[*] ymsong@gist.ac.kr

Abstract: Lithography-free planar structures have been the subject of many studies on structural coloration in recent years because of mass production and large-area applications. Among them, the metal-insulator-metal (MIM) structure follows a subtractive color system. However, the limited gamut of this system hinders a wider application of reflective color filters. We demonstrate a planar metal-insulator-metal-insulator-metal (MIMIM) structure for a tunable dual-resonance mode, by combining each single-resonance mode in MIM structures. By controlling the resonance dips, we obtain standard red/green/blue (sRGB) in the standard color space for modern optical devices. The reflectance spectra, color representation, and fabricated samples verify the dual-resonance tunability and generation of sRGB colors.

1. Introduction

Structural coloration has been intensively studied for key applications in various optical devices. Conventionally, structural coloration has been based on plasmonic nanostructures, thin films, and photonic crystals [1–15]. Due to the advantage of high durability with slim dimension, structural coloration is highly promising for future optical technologies such as bright-field color prints, nanoscale optical filters, and flexible display systems. Furthermore, using these coloring schemes, several studies have been reported with nanofabrication processes such as electron beam lithography or direct laser writing to achieve high color purity and wide color gamut [16–18]. Although such structures enhance color purities, the use of electron beam lithography or direct laser writing and patterning lead to difficulties in mass production and large-scale applications. Nevertheless, for mass production and large-scale applications, lithography-free planar structures such as multilayer thin-film coatings and metal/insulator multilayers have been intensively studied in recent years [19–23]. Among them, the metal-insulator-metal (MIM) resonator has been a strong candidate for color filters due to its strong resonant characteristics. Due to Fabry-Pérot resonance, strong resonance occurs at the insulator layer between the two metals by the multiple round trips of light inside the insulator [24]. Fundamentally, in these thin-film cavities, the resonance is strongly dependent on the thickness of the insulator and the material of the metal layers. With this resonance characteristic, MIM color filters have been studied in diverse combinations of reflective or transmissive types [25–31]. In the reflective type, the color filter with a single resonance mode follows a subtractive color system consisting of cyan, magenta, and yellow (CMY) as the primary colors. In the color space, however, the limited color gamut of CMY, which excludes the additive primary colors consisting of red, green, and blue (RGB), hinders the wider application of reflective color filters. To expand the color gamut beyond the subtractive color determined by a single resonance dip, reflective MIM structures need to be combined to modulate multiple resonances.

#367493 https://doi.org/10.1364/OME.9.003342
Journal © 2019 Received 13 May 2019; revised 27 Jun 2019; accepted 7 Jul 2019; published 12 Jul 2019

Optical Materials EXPRESS

In this work, we present a double-stacked metal-insulator (MIMIM) structure with a dual-resonance mode for various colorations beyond the CMY color range. Compared to the MIM structure which provides a single resonance mode, the proposed scheme permits a tunable dual-resonance mode which can be applied for optical devices that require resonance selectivity. By tuning the resonances, we fabricate MIMIM structures for an optimized RGB coloration nearly close to standard red/green/blue (sRGB), which is in the standard color space for modern optical devices. Optical simulation results support our proposed concept with reflectance contour maps, light absorption and chromaticity diagrams with color representation.

2. Results and discussion

Figure 1(a) presents a schematic representation of the MIMIM structure for primary additive colors (i.e., red, green, and blue) with a metal-insulator (MI) layer and the MIM structure, which are the components of the MIMIM structure. This illustration represents the generation of red, green, and blue (RGB) colors by stacking an additional MI layer on the MIM resonator. The inset shows a cross-sectional view of the MIMIM structure; it illustrates the dual-resonance induced by both the MI layer and the MIM structure. Since the position of the resonance dip is related to the thickness of the insulator by Fabry-Pérot resonance [24], the insulator thicknesses lie within the range of 50-305 nm for generating resonance dips in the visible wavelength range of 380-750 nm. Therefore, these dual-resonance mode structures permit resonance selectivity. Figure 1(b) represents the absorption profiles for a red-colored MIMIM structure (Au (5 nm)/SiO_2 (70 nm)/Ti (5 nm)/SiO_2 (240 nm)/Au) and two different MIM structures, MIM 1 (upper MIM; Ti (15 nm)/SiO_2 (240 nm)/Au) and MIM 2 (lower MIM; Au (5 nm)/SiO_2 (70 nm)/Au). To confirm the existence of a dual-resonance mode in the MIMIM structure, absorption profiles are calculated at 486 nm wavelength, where both the MIM structures generate resonance dips. As the resonances occur at the insulator between two adjacent metals, the top metals of both the MIM structures strongly absorb the light at 486 nm. As shown in Fig. 1(b), both the top metals of the red-colored MIMIM structure also significantly absorb the light. From these results, we infer that the proposed MIMIM structures have a tunable dual-resonance mode and can be applied to optical devices requiring resonance selectivity. Using these properties, RGB colors are provided by the MIMIM structure with different parameters such as the types of metals (i.e., Ag, Au, and Ti) and the insulator thicknesses (Fig. 1(c)). We observe that the color changes from the case of MIM (dashed lines) to MIMIM (solid lines). The structural information is illustrated above the calculated reflectance spectra (i.e., MIM (top left) and MIMIM (top right)). By controlling the insulator thickness, reflectance dips are generated at the proper region for RGB coloration. The corresponding international commission on illumination (CIE) coordinates from the reflectance results are illustrated in Fig. 1(d). It is clear that the colors shift nearly close to sRGB colors by stacking the MI layer on the MIM resonator.

To demonstrate the optical aspects of the proposed structures, rigorous coupled-wave analysis (RCWA) method is used to calculate the reflectance of the structures using commercial software tools (DiffractMOD, RSoft Design Group, USA) [32]. In the calculations, a grid size of 0.1 nm is chosen to calculate the diffraction efficiency, which is enough to stabilize the results. The reflectance spectra and absorption profiles are calculated by averaging the TE and TM polarization modes. The colors and the chromatic information from the calculated and the measured reflectance spectra are estimated using MATLAB (MathWorks, Inc.) [33]. Material dispersions and extinction coefficients are considered to obtain exact outputs. The optical constants of the metal and the insulator materials are obtained from previous studies [34].

Figure 2(a) presents a schematic of the MIM structure with the geometric parameters M_1, I_1, M_2, h_{i1}, and h_{m2}, which represent the metal substrate, insulator, thin metal layer, height of I_1, and height of M_2, respectively. Ag, Au, and Ti are considered as the top metals, and their refractive indices and extinction coefficients are displayed in Fig. 2(b). To confirm the correlation between

Optical Materials EXPRESS

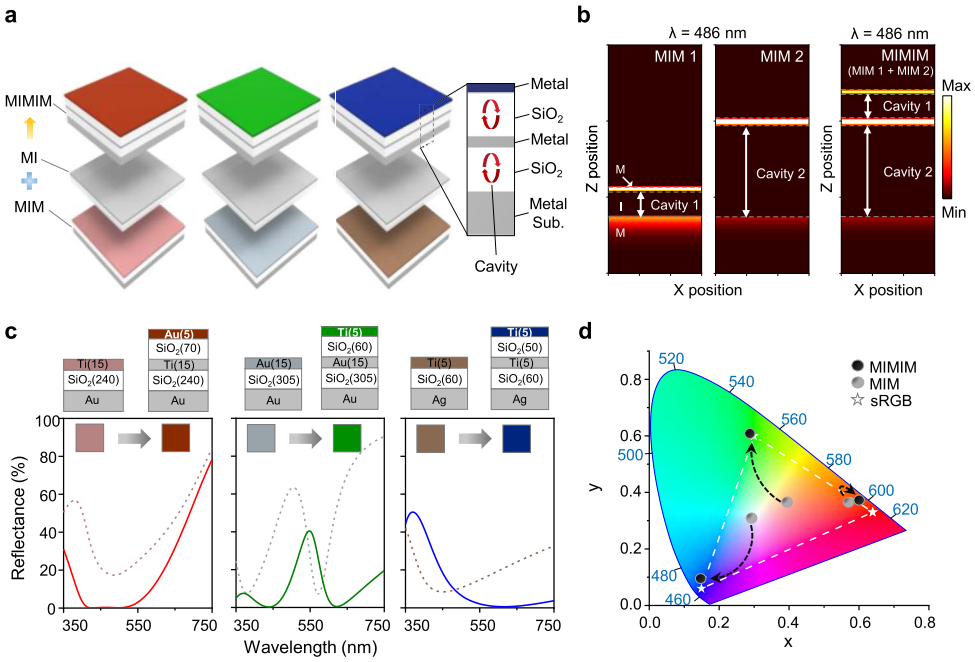

Fig. 1. (a) Schematic illustration of MIMIM structures for RGB coloration, MI layer, and MIM structure. (b) Absorption profiles of MIM 1 (Au (5 nm)/SiO_2 (70 nm)/Au), MIM 2 (Ti (5 nm)/SiO_2 (240 nm)/Au) and red-colored MIMIM (Au (5 nm)/SiO_2 (70 nm)/Ti (5 nm)/SiO_2 (240 nm)/Au) at 486 nm wavelength. (c) MIM and MIMIM structures for RGB coloration, corresponding colors of structures, and calculated reflectance spectra of the MIMIM and MIM structures with different metals (i.e., Au, Ag, and Ti) and different thicknesses of layers. (d) Corresponding chromaticity coordinates from the measured reflectance spectra in (c).

the reflectance dips and the metal-type in the MIM structure, the reflectance contour maps of different top-metal MIM structures (i.e., Ag (5-20 nm)/SiO_2 (120 nm)/Ag, Au (5-20 nm)/SiO_2 (100 nm)/Ag, and Ti (5-20 nm)/SiO_2 (100 nm)/Ag) as a function of h_{m2} from 5 to 20 nm are displayed in Fig. 2(c). SiO_2 is chosen as the lossless insulator layer to ensure a strong resonance. The thickness of the insulator (h_{i1}) is fixed at 120 nm, 100 nm, and 100 nm for Ag, Au, and Ti structures, respectively, in order to compare the shape of each dip at the same wavelength (550 nm). Since a low refractive index contrast with the top metal film (M_2) and air reduces reflection at the air-metal surface, the incident light is transmitted or absorbed more easily into the layer. Thus, a large amount of transmitted light contributes to multiple light circulation at the insulator layers, which enhances the resonance. For this reason, the MIM structure with Ti as the top metal, which has a low refractive index contrast with air broadly in the visible range, generates a deep and broad resonance dip in the visible wavelength range. The reflectance spectra also show that the resonance dip gets deeper and broader as the thickness of the top metal film (h_{m2}) increases. Due to a thicker metal film with a higher reflection from the metal-insulator interface, a stronger resonance occurs in the range of 5-20 nm of h_{m2}. In Fig. 2(d), the effect of the metal substrate (M_1) in the MIM structure is illustrated by reflectance contour plots as a function of the insulator thickness h_{i1}. The top metal (M_2) and the top metal thickness (h_{m2}) in both the cases are chosen as Ag and 10 nm, respectively. Since the metal substrate has the role of a reflector in the MIM structure, Ag and Au (which reflect the light very well in the visible region) are chosen as the metal substrate. It is obvious that the reflectance at shorter wavelengths (left region of the dashed line) drops by changing the substrate from Ag to Au.

Optical Materials EXPRESS

Since the refractive index contrast between Ag and SiO_2 is larger than that between Au and SiO_2 at shorter wavelengths (400-550 nm), a high reflectance is observed broadly in the visible wavelength range at the interface between SiO_2 and Ag bulk (100 nm), while a reflectance drop occurs at shorter wavelengths at the SiO_2-Au bulk interface. Thus, the Au substrate can be used instead of the Ag one when the reflectance drop is required at short wavelengths such as red and green colorations.

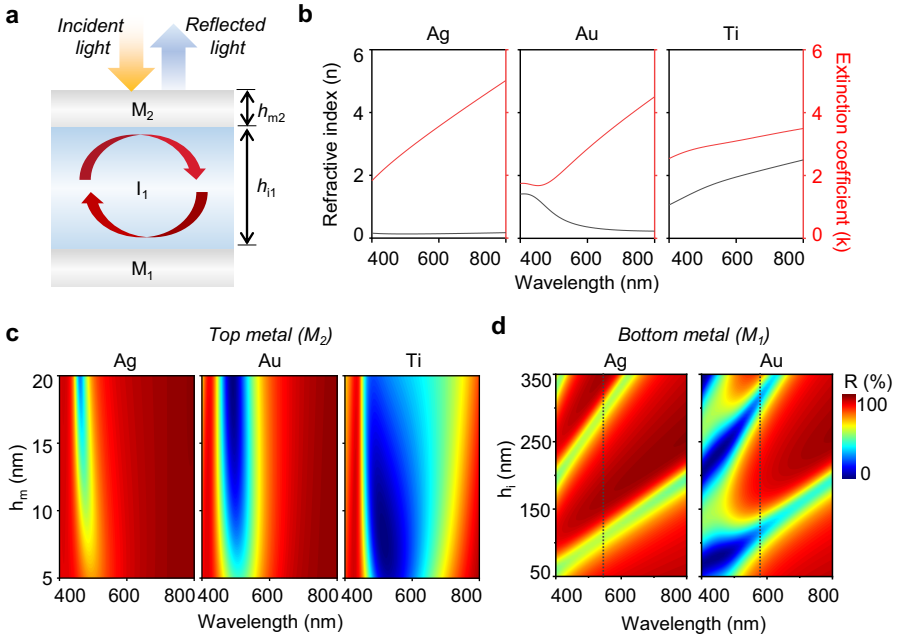

Fig. 2. (a) Schematic illustration of an MIM structure with substrate M_1, insulator I_1, and top metal film M_2 with labeled thicknesses (h_{i1} and h_{m2}). (b) Refractive indices and extinction coefficients of different metals (i.e., Ag, Au, and Ti). (c) Calculated reflectance contour maps of the MIM structures with different top metals as a function of h_{m2} from 5 to 20 nm. (d) Contour plots of reflectance variation for the MIM structures with different M_1 (Ag and Au) as a function of h_{i1}.

Figure 3(a) illustrates a schematic of the MIMIM structure with the parameters M_1, I_1, M_2, I_2, M_3, h_{i1}, h_{m2}, h_{i2}, and h_{m3}, which represent the structural information and the height of the layers. To compare the resonance dips of the MIMIM structures with those of the MIM structures, the reflectance spectra of the MIM and MIMIM structures as a function of insulator thickness are shown in Figs. 3(b) and 3(c). In Fig. 3(b), the simulated results for the lower MIM structure (i.e., Au (10 nm)/SiO_2 (110, 140, 170 nm)/Ag) and the upper MIM structure (i.e., Ag (10 nm)/SiO_2 (90 nm)/Ag) are presented in the left graph, and the result for the MIMIM structure (i.e., Ag (10 nm)/SiO_2 (90 nm)/Au (10 nm)/SiO_2 (110, 140, 170 nm)/Ag) is presented in the right graph. Comparing the MIMIM structure to both the MIM structures, it is observed that the two dips from the MIM structures are also generated in the MIMIM structure. Moreover, a noticeable red-shift of the Au dip is also observed in the MIMIM structure with the increase in SiO_2 thickness (h_{i1}). If both the resonance dips of the MIMIM structure are generated at a large distance from each other in the visible wavelength range, the positions of the MIMIM dips are in good agreement with those of the MIM dips. However, if both the resonance dips are generated close to each other in the visible spectrum, a mutual repulsive interaction occurs between the resonance dips. This interaction is caused by the mutual repulsion of surface plasmon modes [35]. Moreover, Fig. 3(c)

Optical Materials EXPRESS

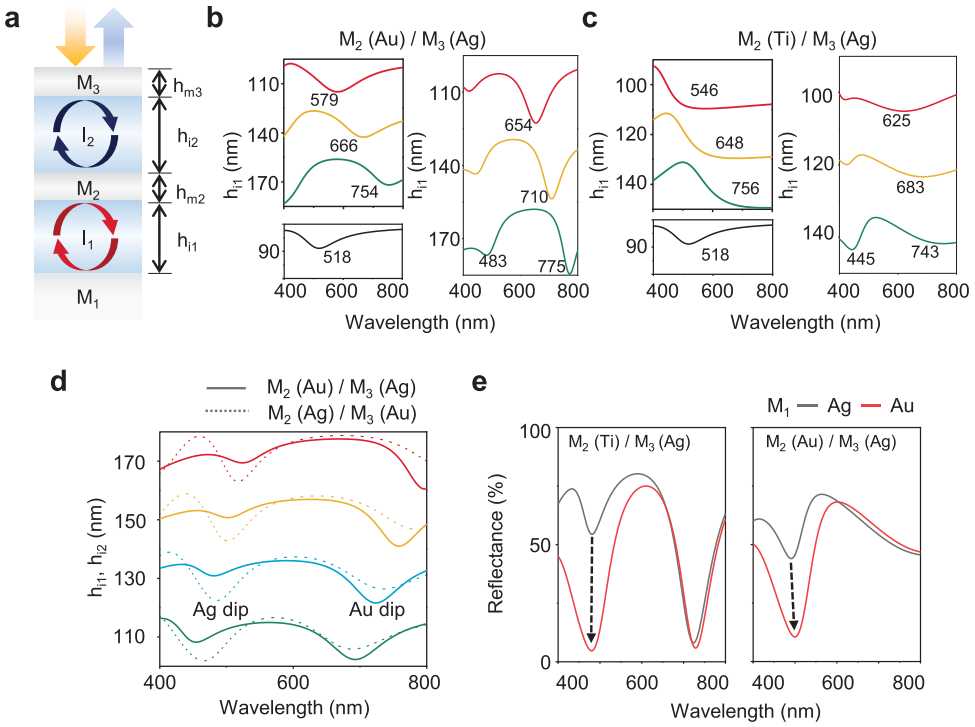

Fig. 3. (a) Schematic illustration of the MIMIM structure with substrate M_1, insulators I_1, I_2, and metal films M_2, M_3 with labeled thicknesses (h_{i1}, h_{i2}, h_{m2}, and h_{m3}). (b) Calculated reflectance spectra of the lower MIM structure (i.e., Au (10 nm)/SiO_2 (110-170 nm)/Ag), upper MIM structure (i.e., Ag (10 nm)/SiO_2 (90 nm)/Ag), and MIMIM structure (i.e., Ag (10 nm)/SiO_2 (90 nm)/Au (10 nm)/SiO_2 (110-170 nm)/Ag). (c) Reflectance spectra of the lower MIM structure (i.e., Ti (10 nm)/SiO_2 (100-140 nm)/Ag), upper MIM structure (i.e., Ag (10 nm)/SiO_2 (90 nm)/Au), and MIMIM structure (i.e., Ag (10 nm)/SiO_2 (90 nm)/Ti (10 nm)/SiO_2 (100-140 nm)/Ag). (d) Calculated reflectance spectra of the switched MIMIM structures (i.e., Ag (10 nm)/SiO_2 (90 nm)/Au (10 nm)/SiO_2 (110-170 nm)/Ag and Au (10 nm)/SiO_2 (110-170 nm)/Ag (10 nm)/SiO_2 (90 nm)/Ag) as a function of h_{i1} and h_{i2}, respectively. (e) Reflectance spectra of the MIMIM structures with different substrates (i.e., Ag and Au).

presents the combined resonance dips of Ag and Ti and the mutual repulsion of surface plasmon modes in MIMIM structures. To investigate the difference between the upper resonance occurring at the second dielectric layer (I_2) and the lower resonance occurring at the first dielectric layer (I_1), we calculate the reflectance spectra of two switched MIMIM structures (i.e., Ag (10 nm)/SiO_2 (90 nm)/Au (10 nm)/SiO_2 (110-170 nm)/Ag (solid lines) and Au (10 nm)/SiO_2 (110-170 nm)/Ag (10 nm)/SiO_2 (90 nm)/Ag (dashed lines)) in Fig. 3(d). Compared to the solid lines, the dashed lines show a deeper Ag dip and a shallower Au dip. These results show that a resonance caused by the lower MIM structure ($M_2/I_1/M_1$) is stronger than that caused by the upper MIM structure ($M_3/I_2/M_2$). Since the resonance caused by the lower MIM structure occurs between the substrate (M_1) and the thin metal (M_2), it results in a strong resonance. Since the resonance caused by the upper MIM structure occurs between two thin metal films (M_2 and M_3), it results in a weak resonance because thin metal films do not reflect light as much as the substrate. This leads to higher transmission and leakage from the upper MIM cavity after reflecting from the top metal layer (M_3). These results indicate the tunability of the reflectance dip depth by switching the

Optical Materials EXPRESS

positions of the MI layers. As displayed in Fig. 3(e), Au substrate also causes a reflectance drop at shorter wavelengths in MIMIM structures. From these results, it is apparent that the metal substrate in MIMIM structures also has the role of a reflector as in the case of MIM structures.

To analyze the proposed structures in terms of coloration, we perform color representations of RGB colored structures as a function of h_{m2} (5-30 nm) and h_{i1} (120-240 nm (red), 185-305 nm (green), 50-170 nm (blue)), as displayed in Fig. 4(a). These structures are the same as the proposed structures presented in Fig. 1(c) (i.e., red: Au (5 nm)/SiO_2 (70 nm)/Ti (5-30 nm)/SiO_2 (120-240 nm)/Au, green: Ti (5 nm)/SiO_2 (60 nm)/Au (5-30 nm)/SiO_2 (185-305 nm)/Au, and blue: Ti (5 nm)/SiO_2 (50 nm)/Ti (5 nm)/SiO_2 (60 nm)/Ag). The other parameters (h_{i2}, h_{m1}) are kept constant except for h_{i1} and h_{m2}. As the reflectance should decrease at shorter wavelengths to obtain red and green color, Au is used as the metal substrate, while the Ag substrate is used for the blue-colored structure. Furthermore, Ti and Au are chosen as the top metal layers of the RGB colored structures to create a proper resonance dip width and depth. From these color representations, we observe that a variation in insulator thickness (h_{i1}) causes significant color changes due to the shift in the resonance dip in the visible range. On the other hand, a variation in metal thickness (h_{m2}) causes small color changes since it affects only the depth of the resonance dip. Figure 4(b) presents the color difference ΔE of the RGB colored MIMIM structures as a function of the thickness of the first dielectric (h_{i1}) and the second dielectric (h_{i2}). ΔE is a mathematical description of the Euclidean distance between colors produced by the MIMIM structures and the sRGB colors in CIE 1976 coordinates, demonstrating that the proposed structures are optimized to sRGB colors through quantified color examination [36].

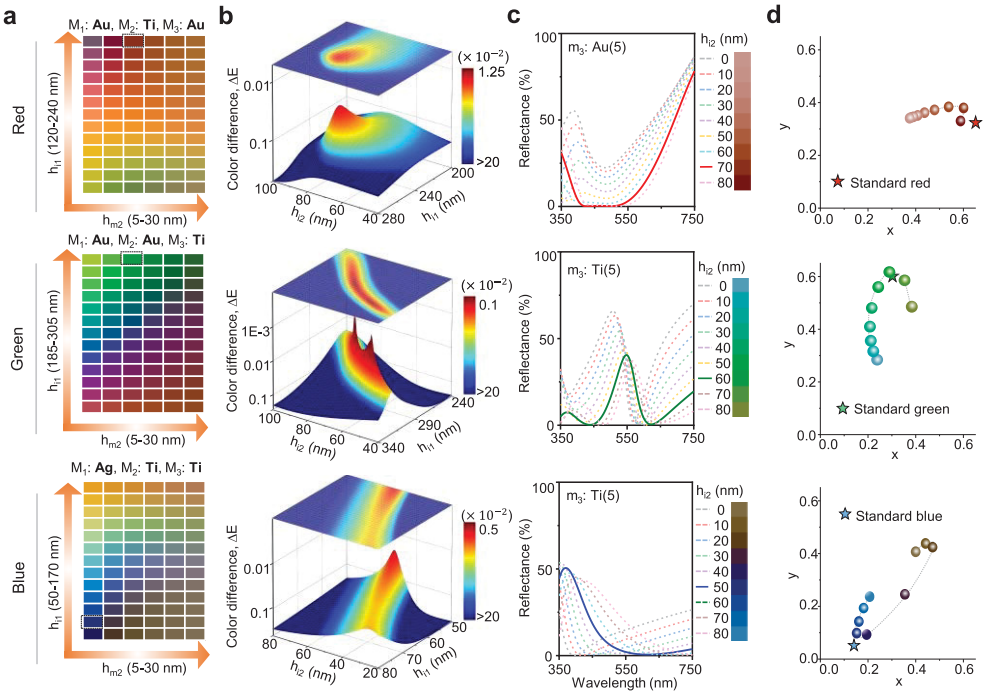

Fig. 4. (a) Color representations of the red structure (Au (5 nm)/SiO_2 (70 nm)/Ti (15 nm)/SiO_2 (240 nm)/Au), green structure (Ti (5 nm)/SiO_2 (60 nm)/Au (15 nm)/SiO_2 (305 nm)/Au), and blue structure (Ti (5 nm)/SiO_2 (50 nm)/Ti (5 nm)/SiO_2 (60 nm)/Ag) with different h_{i1} and h_{m2}. (b) 3D contour map of color purity as a function of h_{i1} and h_{i2}. (c) Reflectance spectra for the RGB structures with different h_{i2} as a function of h_{i2} (0-80 nm). (d) Chromaticity diagrams corresponding to (c).

Optical Materials EXPRESS

Since a small color difference means a high color similarity between two colors, we choose the smallest values of ΔE as the optimized conditions for standard red, green, or blue colors. Figure 4(c) presents the calculated reflectance spectra of the RGB colored MIMIM structures as a function of h_{i2}. Due to the mutual repulsion of the two resonances, the resonance dip caused by M_2 also shifts slightly to a larger wavelength with increasing h_{i2}. By controlling the thickness of the insulator (h_{i2}), it is possible to generate red, green, and blue colors as shown in the right side of the reflectance spectra. Figure 4(d) presents the chromaticity diagrams obtained from the reflectance measurements in Fig. 4(c). This proves that the optimized structures generate high-purity RGB colors since those are close to the sRGB values.

We experimentally fabricated and measured the reflectance spectra and chromaticity coordinates. An electron-beam evaporator (KVE-E2000, Korea Vacuum Tech., Ltd., Korea) was used to fabricate the RGB colored MIMIM samples. Figure 5(a) presents the scanning electron microscopy (SEM) images of experimental red (i*), green (ii*), and blue (iii*) samples under 50,000 times magnification. As observed in SEM images, all three RGB samples exhibit 5 layers as we designed. The calculated and the measured RGB reflectance spectra are plotted in Figs. 5(b) and 5(c), respectively. The measured spectra were obtained using a UV-Vis-NIR spectrophotometer (Cary 500, Varian, USA) at a normal angle of incidence with a tungsten-halogen lamp source. The simulated reflectance spectra for RGB colors also show a good qualitative agreement with the measured reflectance spectra since the shapes of the reflectance spectra and the positions of the dips are similar to each other. In details, there are slight differences between calculations and experiments in red (i and i*) and green (ii and ii*) samples. These subtle discrepancies in the measurement process could be caused by optical properties of reference reflector (i.e., Ag substrate) to obtain the reflectance [34]. Also, for universality, since conventional optical constants from commonly known references [34] were used in the calculation of MIMIM

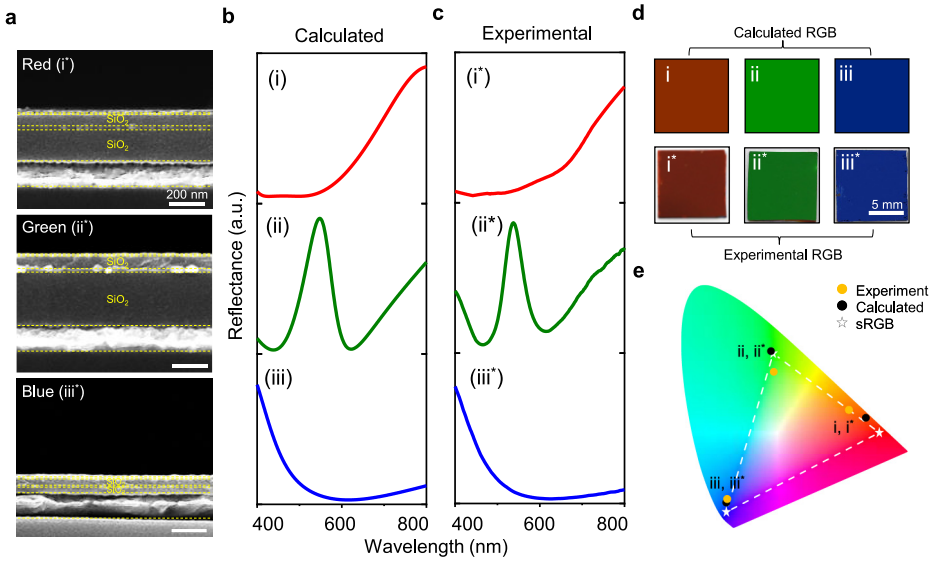

Fig. 5. (a) Scanning electron microscope (SEM) images of experimental red (i.e., Au(5)/SiO_2(70)/Ti(15)/SiO_2(240)/Au), green (i.e., Ti(5)/SiO_2(60)/Au(15)/SiO_2(305)/Au), and blue (i.e., Ti(5)/SiO_2(50)/Ti(5)/SiO_2(60)/Ag) samples (×50,000 original magnification). (b) Reflectance spectra of the calculated RGB structures in (a). (c) Measured reflectance spectra of the experimental RGB samples in (a). (d) Calculated RGB colors (i, ii, iii) and experimental RGB colors (i*, ii*, iii*) for MIMIM structures. (e) Corresponding chromaticity coordinates of (c).

Optical Materials EXPRESS

structures, optical properties of fabricated samples may not be matched perfectly with calculation results. For the red-colored structures (i and i*), the dominant reflectance in the red region (620-740 nm) produces a red color (Fig. 5(d), i and i*). For the green-colored structures (ii and ii*), the reflectance peak is in the green region (500-570 nm) to render a green color (Fig. 5(d), ii and ii*), and for the blue-colored structures (iii and iii*), the dominant reflectance lies in the blue region (450-490 nm) in agreement with the observed blue color (Fig. 5(d), iii and iii*). Figure 5(d) presents the images of the experimental samples and the estimated RGB colors. We note that the real images and the estimated colors are in significantly good agreement with each other. The chromatic values of the fabricated samples and the calculated values are shown in Fig. 5(e). The experimental data for red (i*), green (ii*), and blue (iii*) in the CIE color space are comparable to the calculated data for red (i), green (ii), and blue (iii) colors, respectively. These results demonstrate the feasibility of high-purity RGB colored MIMIM structures by choosing proper metals and layer thicknesses without any lithography techniques, thereby enabling large-scale and mass production.

3. Conclusions

In summary, we presented a large-scale, lithography-free, and fine-tunable dual-resonance planar MIMIM nanostructure. We inferred that double-stacked metal-insulator layers create two resonances, which can be tuned across the visible spectrum by altering the geometry such as the insulator thickness. We also studied the applicability of the well-known metal materials (i.e., Au, Ag, and Ti) as thin metal films and metal substrates and confirmed that the shapes of the reflectance dips depend on the metal-type by comparing the refractive indices of the metals. Significantly, these properties permit wavelength selectivity, which enables us to generate high-purity colors by controlling the resonance dip. As a demonstration, we successfully generated high-purity colors nearly close to sRGB colors by optimizing the conditions of insulator thicknesses, types of metals, and metal thicknesses. Furthermore, the results from the fabricated samples were comparable to the calculated results, including those for reflectance and color representation. Using this approach, we believe that the dual-resonance tunability and high color purity features of the proposed structures can be used in future color applications such as colored solar cell, decorative devices, large-area with high-resolution color rendering, and wavelength-selective photodetectors. In addition, for practical applications, we expect that the proposed structure can be applied as color pixels of different colors using photolithography or shadow mask technique [22,37]. Alternatively, color halftoning can also be exploited to represent various colors with the proposed MIMIM structures of three primary colors (i.e., red, green, and blue) as the representative result in our study [38].

Funding

Gwangju Institute of Science and Technology (GIST) (KETEP); National Research Foundation of Korea (NRF) (NRF-2018H1A2A1060954, NRF-2018R1A4A1025623); Agency for Defense Development (ADD) (UD170079FD); National Research Foundation of Korea (NRF) (NRF-2017M3D1A1039288).

Disclosures

The authors declare that there are no conflicts of interest related to this article.

References

1. T. Xu, Y.-K. Wu, X. Luo, and L. J. Guo, "Plasmonic nanoresonators for high-resolution colour filtering and spectral imaging," Nat. Commun. **1**(1), 59 (2010).
2. J. Guo, C. M. Huard, Y. Yang, Y. J. Shin, K. Lee, and L. J. Guo, "ITO-free, compact, color liquid crystal devices using integrated structural color filters and graphene electrodes," Adv. Opt. Mater. **2**(5), 435–441 (2014).

Optical Materials EXPRESS

3. Y. S. Do, J. H. Park, B. Y. Hwang, S. Lee, B. Ju, and K. C. Choi, "Plasmonic color filter and its fabrication for large-area applications," Adv. Opt. Mater. **1**(2), 133–138 (2013).
4. R. Mudachathi and T. Tanaka, "Up scalable full colour plasmonic pixels with controllable hue, brightness and saturation," Sci. Rep. **7**(1), 1199 (2017).
5. F. Cheng, J. Gao, T. S. Luk, and X. Yang, "Structural color printing based on plasmonic metasurfaces of perfect light absorption," Sci. Rep. **5**(1), 11045 (2015).
6. R. W. Sabnis, "Color filter technology for liquid crystal displays," Displays **20**(3), 119–129 (1999).
7. H. N. Umh, S. Yu, Y. H. Kim, S. Y. Lee, and J. Yi, "Tuning the structural color of a 2D photonic crystal using a bowl-like nanostructure," ACS Appl. Mater. Interfaces **8**(24), 15802–15808 (2016).
8. Z. Li, A. W. Clark, and J. M. Cooper, "Dual color plasmonic pixels create a polarization controlled nano color palette," ACS Nano **10**(1), 492–498 (2016).
9. G. Si, Y. Zhao, J. Lv, M. Lu, F. Wang, H. Liu, N. Xiang, T. J. Huang, A. J. Danner, and J. Teng, "Reflective plasmonic color filters based on lithographically patterned silver nanorod arrays," Nanoscale **5**(14), 6243–6248 (2013).
10. Y. Li, D. Luo, and Z. H. Peng, "Full-color reflective display based on narrow bandwidth templated cholesteric liquid crystal film," Opt. Mater. Express **7**(1), 16–24 (2017).
11. Y. J. Kim, Y. J. Yoo, G. J. Lee, D. E. Yoo, D. W. Lee, V. Siva, H. Song, I. S. Kang, and Y. M. Song, "Enlarged color gamut representation enabled by transferable silicon nanowire arrays on metal-insulator-metal films," ACS Appl. Mater. Interfaces **11**(12), 11849–11856 (2019).
12. Y. J. Yoo, J. H. Lim, G. J. Lee, K.-I. Jang, and Y. M. Song, "Ultra-thin films with highly absorbent porous media fine-tunable for coloration and enhanced color purity," Nanoscale **9**(9), 2986–2991 (2017).
13. K.-T. Lee, D. Kang, H. J. Park, D. H. Park, and S. Han, "Design of polarization-independent and wide-angle broadband absorbers for highly efficient reflective structural color filters," Materials **12**(7), 1050 (2019).
14. S. Song, X. Ma, M. Pu, X. Li, K. Liu, P. Gao, Z. Zhao, Y. Wang, C. Wang, and X. Luo, "Actively tunable structural color rendering with tensile substrate," Adv. Opt. Mater. **5**(9), 1600829 (2017).
15. M. Song, X. Li, M. Pu, Y. Guo, K. Liu, H. Yu, X. Ma, and X. Luo, "Color display and encryption with a plasmonic polarizing metamirror," Nanophotonics **7**(1), 323–331 (2018).
16. B. Yang, W. Liu, Z. Li, H. Cheng, D.-Y. Choi, S. Chen, and J. Tian, "Ultra-highly saturated structural colors enhanced by multipolar-modulated metasurfaces," Nano Lett. **19**(7), 4221–4228 (2019).
17. Z. Dong, J. Ho, Y. F. Yu, Y. H. Fu, R. Paniagua-Dominguez, S. Wang, A. I. Kuznetsov, and J. K. W. Yang, "Printing beyond sRGB color gamut by mimicking silicon nanostructures in free-space," Nano Lett. **17**(12), 7620–7628 (2017).
18. S. U. Lee and B.-K. Ju, "Wide-gamut plasmonic color filters using a complementary design method," Sci. Rep. **7**(1), 40649 (2017).
19. C. Yang, W. Shen, Y. Zhang, K. Li, X. Fang, X. Zhang, and X. Liu, "Compact multilayer film structure for angle insensitive color filtering," Sci. Rep. **5**(1), 9285 (2015).
20. Y.-T. Yoon and S.-S. Lee, "Transmission type color filter incorporating a silver film based etalon," Opt. Express **18**(5), 5344–5349 (2010).
21. C.-S. Park, V. R. Shrestha, S.-S. Lee, and D.-Y. Choi, "Trans-reflective color filters based on a phase compensated etalon enabling adjustable color saturation," Sci. Rep. **6**(1), 25496 (2016).
22. M. A. Kats, R. Blanchard, P. Genevet, and F. Capasso, "Nanometre optical coatings based on strong interference effects in highly absorbing media," Nat. Mater. **12**(1), 20–24 (2013).
23. S. S. Mirshafieyan and D. A. Gregory, "Electrically tunable perfect light absorbers as color filters and modulators," Sci. Rep. **8**(1), 2635 (2018).
24. Z. Li, S. Butun, and K. Aydin, "Large-area, lithography-free super absorbers and color filters at visible frequencies using ultrathin metallic films," ACS Photonics **2**(2), 183–188 (2015).
25. K. Diest, J. A. Dionne, M. Spain, and H. A. Atwater, "Tunable color filters based on metal− insulator− metal resonators," Nano Lett. **9**(7), 2579–2583 (2009).
26. G. J. Lee, Y. J. Kim, H. M. Kim, Y. J. Yoo, and Y. M. Song, "Colored, daytime radiative coolers with thin-film resonators for aesthetic purposes," Adv. Opt. Mater. **6**(22), 1800707 (2018).
27. Z. Li, S. Butun, and K. Aydin, "Lithography-free transmission filters at ultraviolet frequencies using ultra-thin aluminum films," J. Opt. **18**(6), 065006 (2016).
28. J. H. Han, D. Kim, T.-W. Lee, Y. Jeon, H. S. Lee, and K. C. Choi, "Color purifying optical nanothin film for three primary colors in optoelectronics," ACS Photonics **5**(8), 3322–3330 (2018).
29. S. Dutta Choudhury, R. Badugu, K. Ray, and J. R. Lakowicz, "Directional emission from metal–dielectric–metal structures: effect of mixed metal layers, dye location, and dielectric thickness," J. Phys. Chem. C **119**(6), 3302–3311 (2015).
30. M. Aalizadeh, A. E. Serebryannikov, A. Khavasi, G. A. E. Vandenbosch, and E. Ozbay, "Toward electrically tunable, lithography-free, ultra-thin color filters covering the whole visible spectrum," Sci. Rep. **8**(1), 11316 (2018).
31. K. Mao, W. Shen, C. Yang, X. Fang, W. Yuan, Y. Zhang, and X. Liu, "Angle insensitive color filters in transmission covering the visible region," Sci. Rep. **6**(1), 19289 (2016).
32. M. G. Moharam, "Coupled-wave analysis of two-dimensional dielectric gratings," Proc. SPIE **0883**, 8–12 (1988).
33. T. Smith and J. Guild, "The CIE colorimetric standards and their use," Trans. Opt. Soc., London **33**(3), 73–134 (1931).

Optical Materials EXPRESS

34. A. D. Rakić, A. B. Djurišić, J. M. Elazar, and M. L. Majewski, "Optical properties of metallic films for vertical-cavity optoelectronic devices," Appl. Opt. **37**(22), 5271–5283 (1998).
35. E. N. Economou, "Surface plasmons in thin films," Phys. Rev. **182**(2), 539–554 (1969).
36. W. S. Mokrzycki and M. Tatol, "Color difference Delta E-A survey," Mach. Graph. Vis. **20**(4), 383–411 (2011).
37. A. Tixier, Y. Mita, J. P. Gouy, and H. Fujita, "A silicon shadow mask for deposition on isolated areas," J. Micromech. Microeng. **10**(2), 157–162 (2000).
38. H. Haneishi, T. Suzuki, N. Shimoyama, and Y. Miyake, "Color digital halftoning taking colorimetric color reproduction into account," J. Electron. Imaging **5**(1), 97–107 (1996).